metals

MDPI

Article

The Preparation, Corrosion Resistance and Formation Mechanism of a New-Type Mo-Based Composite Conversion Coating on 6061 Aluminum Alloy

Xuzheng Qian [1,2], Feng Huang [2], Xu Teng [1], Yiqun Wang [2], Yingsong Fang [2], Jingjing Pan [2], Wenhao Wang [3], Yingpeng Li [1] and Wen Zhan [1,3,*]

[1] Haixi (Fujian) Institute, China Academy of Machinery Science and Technology Group Co., Ltd., Sanming 365500, China
[2] College of Mechanical and Electrical Engineering, Huangshan University, Huangshan 245041, China
[3] State Key Laboratory of Special Surface Protection Materials and Application Technology, Wuhan Research Institute of Materials Protection, Wuhan 430030, China
* Correspondence: zhanwen-0000@163.com

Abstract: This paper aims to explore a new-type Mo-based composite conversion coating on 6061 aluminum alloy, systematically evaluate its corrosion resistance, and further reveal the formation mechanism. The effects of pH, conversion time (CTI) and H_2ZrF_6 content on the corrosion resistance were determined by the dropping test and electrochemical tests, and the average corrosion rate (ACR) in neutral 3.5 wt.% NaCl solution under different temperatures was calculated by the immersion test. The micro-morphology and phase compositions were systematically investigated by SEM, EDS and XPS. The results showed that the optimal pH and CTI were 4.5 and 12 min respectively, and the most suitable addition amount of H_2ZrF_6 was 1.2 mL/L. The micro-morphology of the Mo/Ti/Zr conversion coating (MoTiZrCC) under the best conversion condition was relatively smooth and dense, and its phase compositions mainly consisted of MoO_3, Mo_2O_5, TiO_2, ZrO_2 and Al_2O_3. The MoTiZrCC could significantly improve corrosion resistance with the lower icorr and higher R_p, and the ACR of the MoTiZrCC could be reduced to 16.7% of the Al alloy matrix. Additionally, based on the above results, the formation mechanism for the MoTiZrCC was logically deduced.

Keywords: Al alloy matrix; MoTiZrCC; corrosion resistance; formation mechanism

check for updates

Citation: Qian, X.; Huang, F.; Teng, X.; Wang, Y.; Fang, Y.; Pan, J.; Wang, W.; Li, Y.; Zhan, W. The Preparation, Corrosion Resistance and Formation Mechanism of a New-Type Mo-Based Composite Conversion Coating on 6061 Aluminum Alloy. *Metals* **2023**, *13*, 168. https://doi.org/10.3390/met13010168

Academic Editor: David M. Bastidas

Received: 29 November 2022
Revised: 6 January 2023
Accepted: 11 January 2023
Published: 13 January 2023

Copyright: © 2023 by the authors. Licensee MDPI, Basel, Switzerland. This article is an open access article distributed under the terms and conditions of the Creative Commons Attribution (CC BY) license (https://creativecommons.org/licenses/by/4.0/).

1. Introduction

In recent years, the automobile, as an important means of transportation, has become an indispensable necessity for every family. However, its popularity has also caused a serious waste of resources and environmental pollution [1,2]. It is reported that the consumption of automobile oil accounts for about half of the total oil consumption, and even more than half of the pollutants in the atmosphere originate from automobile exhaust emission [3]. Nevertheless, if the automobile body weight can be reduced by 10%, then the oil consumption can be decreased by 6~8% and pollutant emission can be cut down by 4~6% [4]. Therefore, one effective strategy for energy conservation and emission reduction is a lightweight automobile body.

The aluminum alloy can be well substituted for steel and effectively reduce the automobile body weight due to its low density, high specific strength, good ductility and easy processing [5,6]. Indeed, many models have adopted an aluminum alloy body, such as Tesla Model S, NextEV ES8, etc. However, the long-term direct use of aluminum alloy, especially under high salt, high humidity, acid rain and other severe climatic conditions, can produce various forms of corrosion, thus affecting its service performance [7–9]. In order to improve its corrosion resistance and adhesion to the outer paint, the conventional pretreatment of the automobile body is phosphating process, yet that process is only applicable to steel. Because of

the toxic effect of Al^{3+} on the phosphating solution, the film-forming ability of the aluminum alloy significantly decreases over the course of phosphorylation [10–12]. Therefore, it is of great significance to select a suitable pretreatment process for the aluminum alloy body.

The conversion coating process (CCP), which has the advantages of a simple operation, low energy consumption, and good film-forming ability for large-area and complex-shaped workpieces [13,14], is widely used in aluminum alloy surface treatment. Currently, the mature CCP used in the market is chromate CCP [15–17]. However, Cr^{6+} in chromate CCP is highly toxic, carcinogenic and bioaccumulative, causing great damage and a serious threat to the environment and human health [18,19]. Many countries have restricted its use [20], and the emergence of new alternative processes has become very important [21,22]. Mo and Cr belong to the same family, and thus their chemical properties are similar, while the author's previous studies have shown that a Mo-based conversion coating has good corrosion resistance [23]. Additionally, Mo has a low toxicity and is even an essential trace element for the human body. Consequently, an environmental-friendly Mo-based composite CCP is one of the most promising processes to replace the conventional chromate CCP.

Here, a new-type Mo-based composite conversion coating (MoTiZrCC) was explored, and the influences of the conversion parameters (pH and conversion time) and H_2ZrF_6 content on its corrosion resistance were systematically investigated. The correlations among the morphology, elemental distribution, phase compositions and corrosion resistance were fully discussed, and the formation mechanisms of the MoTiZrCC were further revealed. The research results aim to provide the important theoretical and technical support for the use of the aluminum alloy.

2. Materials and Methods

Commercially available 6061 aluminum alloy was used as the Al alloy matrix in this study, and the detailed chemical composition is listed in Table 1.

Table 1. Chemical composition of 6061 aluminum alloy (wt.%).

Element	Cu	Mg	Mn	Fe	Si	Zn	Cr	Al
Content/%	0.16	1.01	0.45	0.31	0.55	0.08	0.05	Bal.

Specimens were sequentially abraded with emery paper from 400 to 1200 grits, then washed by 5% ZHM-1026 (a commercial acid degreasing treatment solution, purchased from Wuhan Research Institute of Materials Protection, China) to remove the naturally formed oxide film and grease, and finally thoroughly rinsed three times with distilled water. Subsequently, the specimens were rapidly immersed in conversion solution to prepare the conversion coating (CC). The conversion parameters were that the pH value was from 3.0 to 5.5, adjusted by ammonia; the conversion time (CTI) was in the range of 1–24 min and the conversion temperature was 40 °C. The conversion solution formula of the MoTiCC and optimal MoTiZrCC is shown in Table 2. In addition, 0–2.0 g/L Na_3VO_4 was added into the MoTiCC formula to determine the influence of the vanadium ion on its corrosion resistance.

Table 2. The formula of the conversion solution.

Sample	$Na_2MoO_4 \cdot 2H_2O$ (g/L)	H_2TiF_6 (mL/L)	$(NaPO_3)_6$ (g/L)	H_2ZrF_6 (mL/L)
MoTiCC	2.8	1.8	0.5	0
MoTiZrCC	2.8	1.8	0.5	1.2

The corrosion resistance of the CC was examined by a copper sulfate dropping corrosion test, and the time it took for the droplets to change from sky blue to light red was recorded. The longer the dropping time was, the better the corrosion resistance was. The drop solution was composed of 13 mL/L HCl, 41 g/L $CuSO_4 \cdot 5H_2O$, and 35 g/L NaCl.

The electrochemical test was carried out using potentiodynamic polarization curves with a CHI660D electrochemical workstation. The test specimens were pre-immersed in a 3.5 wt.% NaCl solution for 15 min to achieve the constant open-circuit potential, and the area exposed to the corrosive medium was 1 cm^2. The potentiodynamic polarization curves were acquired from −2.0 to +0.5 V with a scan rate of 0.01 V/s.

The specimens to be tested were immersed in neutral 3.5 wt.% NaCl solution at five immersion temperatures (20, 30, 40, 50 and 60 °C), and the total immersion time was 144 h. The sampling time points were set as 24, 48, 72, 96, 120 and 144 h at each immersion temperature, and three specimens of the Al alloy matrix and MoTiZrCC were separately taken out at each sampling point. Afterward, the loose corrosion products on their surface were thoroughly removed, then weighed, and lastly the average corrosion rate (*ACR*) was calculated by Equation (1).

$$ACR = \frac{M_0 - M_1}{A \cdot T} \quad (1)$$

where M_0 is the original weight, M_1 is the weight after the removal of surface corrosion products, A is the surface area, and T is the immersion time.

The microscope morphology of the MoTiZrCC was investigated by scanning electron microscopy (SEM) with an acceleration voltage of 15 kV, and its compositions and element distribution were measured using energy dispersive spectrometry (EDS). Furthermore, the valence state and the types of compounds were qualitatively analyzed via X-ray photoelectron spectroscopy (XPS) with a monochromated Al Kα source (1486.6 eV), and the charging effect was calibrated by using the C1s peak at 284.6 eV as the standard for the tested specimens.

3. Results and Discussion

3.1. Effect of pH and CTI

Based on a large number of previous experiments, the main film-forming agent was determined as 2.8 g/L $Na_2MoO_4 \cdot 2H_2O$, 1.8 mL/L H_2TiF_6, and 0.5 g/L $(NaPO_3)_6$, and the comprehensive effect of the pH and CTI on corrosion resistance is shown in Table 3. It can be seen that the general trend of the dropping time increased first and then decreased with the rise in pH, indicating that either too high or too low a pH value causes a decrease in corrosion resistance. When the pH value is too low, it is not easy for the F^- dissolving aluminum to reach the sedimentation threshold of the Mo/Ti oxide, even if the generated Mo/Ti oxide is also dissolved. That is to say, it is difficult to form the complete conversion coating in such growth conditions [24]. Conversely, a high pH value can lead to the rapid deposition of Mo^{4+} and Ti^{4+} in the solution. However, owing to the large internal growth stress, the generated CC easily becomes loose and uneven, thus affecting its corrosion resistance. Consequently, the suitable pH value is about 4.5.

The CTI is closely related to the formation process of the CC, and its influence on corrosion resistance is also displayed in Table 3. Clearly, the dropping time also increased at first and then declined with the increase in CTI. In general, a sufficient CTI can ensure the formation of a complete CC with good corrosion resistance. However, with the continuous increase in CTI, the growth of the CC is accompanied by high internal growth stress, which instead leads to a decrease in the corrosion resistance. To sum up, the optimal pH and CTI were 4.5 and 12 min respectively, with the longest dropping time being 62 s.

3.2. Effect of Na_3VO_4 and H_2ZrF_6 Content

In order to improve the corrosion resistance to a greater extent, the Na_3VO_4 and H_2ZrF_6 were introduced into the conversion liquid with the optimal conversion parameters (pH: 4.5 and CTI: 12 min), respectively, and the relationship between the addition amount and dropping time is shown in Figure 1. Apparently, the dropping time slightly rose with the increase in Na_3VO_4 content, and even experienced some decline. At the Na_3VO_4 content of 0.8 g/L, the dropping time reached its maximum value of 69 s, which was barely

7 s higher than that without the addition of Na_3VO_4. Hence, the addition of Na_3VO_4 had little effect on the improvement of corrosion resistance.

Table 3. Comprehensive influence of the relevant conversion parameters of pH and CTI on dropping time.

PH \ CTI (min)	1	4	8	12	16	20	24
3	33	41	43	36	32	26	20
3.5	29	36	40	33	44	35	27
4	35	46	50	41	48	40	45
4.5	28	43	58	62	54	50	52
5	21	27	25	39	44	49	40
5.5	18	22	33	31	38	43	47

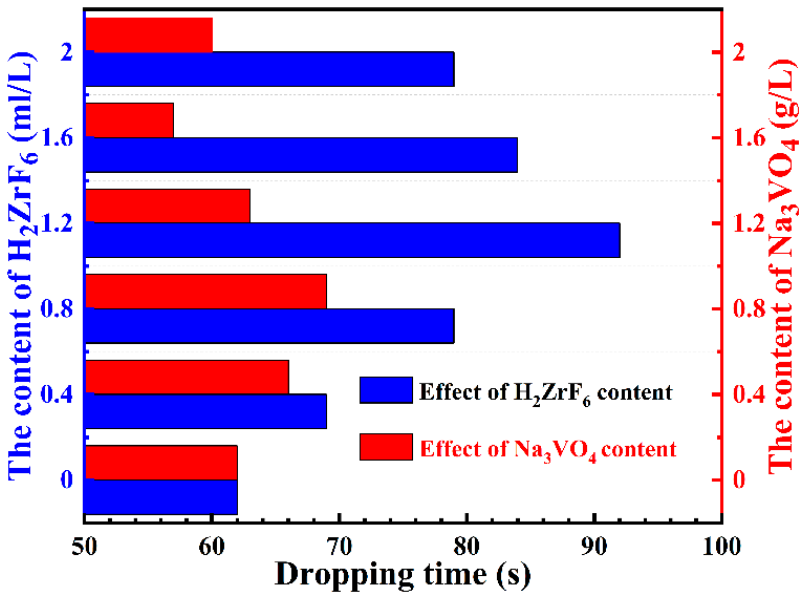


Figure 1. The influence of Na_3VO_4 and H_2ZrF_6 content on the dropping time.

Fortunately, the dropping time significantly increased with the addition of H_2ZrF_6 and the corrosion resistance was greatly improved. It can be seen that the H_2ZrF_6 content of 1.2 mL/L corresponded to the longest dropping time of 92 s, which was 48.38% higher than that of without the addition of H_2ZrF_6. Therefore, the addition of H_2ZrF6 contributed greatly to the improvement of corrosion resistance, and the most appropriate addition amount was 1.2 mL/L.

3.3. Electrochemical Analysis

Figure 2a displays potentiodynamic polarization curves of the Al alloy matrix, MoTiCC and MoTiZrCC in a neutral 3.5 wt.% NaCl solution, and the relevant fitting values of corrosion potential (E_{corr}) and corrosion current density (i_{corr}) are exhibited in Figure 2b. As an important thermodynamic parameter, the E_{corr} values of the Al alloy matrix and MoTiCC were −1.06 and −0.97 V, respectively, whereas that of the MoTiZrCC, shifting towards the more positive direction, was −0.84 V, implying that the MoTiZrCC has lower corrosion susceptibility.

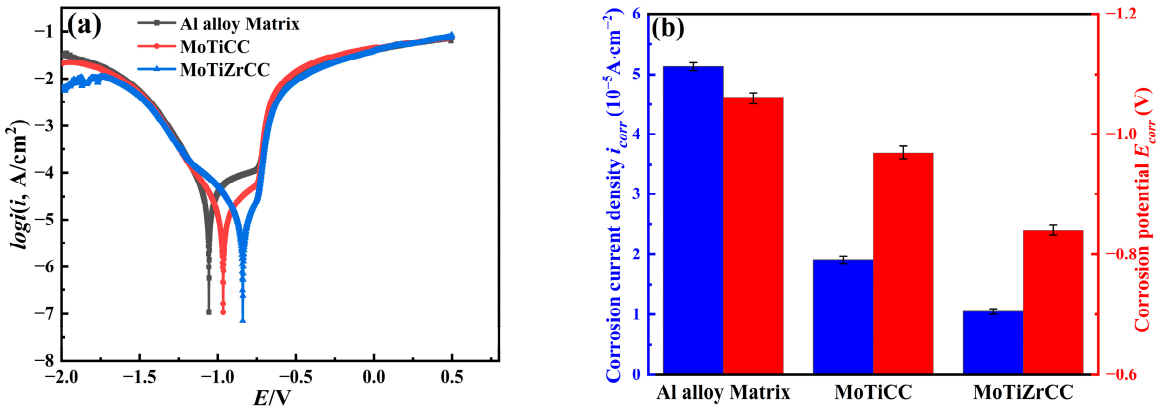


Figure 2. (**a**) Potentiodynamic polarization curves of the Al alloy matrix, MoTiCC and MoTiZrCC; (**b**) is the fitting value of E_{corr} and i_{corr}.

The corrosion current density (i_{corr}) is a representative kinetic parameter to assess the corrosion rate, and a higher value of i_{corr} means poor corrosion resistance. The i_{corr} values of the Al alloy matrix, MoTiCC and MoTiZrCC were 5.13×10^{-5}, 1.91×10^{-5} and 1.04×10^{-5} A/cm^2, respectively. It is quite evident that the i_{corr} of the MoTiZrCC was the lowest, indicating that the MoTiZrCC can significantly reduce the corrosion rate [25,26].

As a supplement, the polarization resistance (R_p) was introduced in order to characterize comprehensive effect of the interfacial charge transfer resistance and CC resistance, and further used to evaluate the drag force of the corrosion behavior. The R_p was calculated using the following formula [27,28]:

$$R_p = \frac{b_a \cdot b_c}{2.3 \times (b_a + b_c)} \cdot \frac{1}{i_{corr}} \quad (2)$$

where b_a is the anodic Tafel slope, b_c is the cathodic Tafel slope, and i_{corr} is the corrosion current density. It can be seen from Figure 3 that the R_p of the MoTiCC and MoTiZrCC were significantly increased compared with the Al alloy matrix. In particular, the R_p of the MoTiZrCC was higher by one order of magnitude than that of the Al alloy matrix. The results indicate that the MoTiZrCC can inhibit the interfacial charge transfer caused by the surface corrosion reaction and provide a barrier to prevent the penetration of the corrosion medium. In a nutshell, the MoTiZrCC has a lower corrosion sensitivity and corrosion rate, as well as a higher drag force of the corrosion reaction.

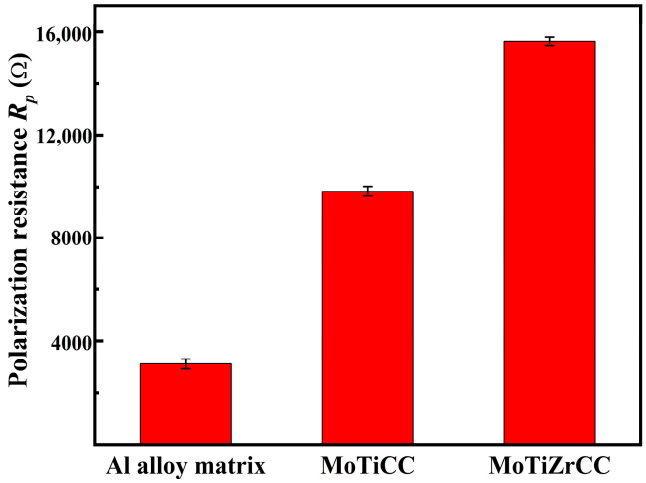
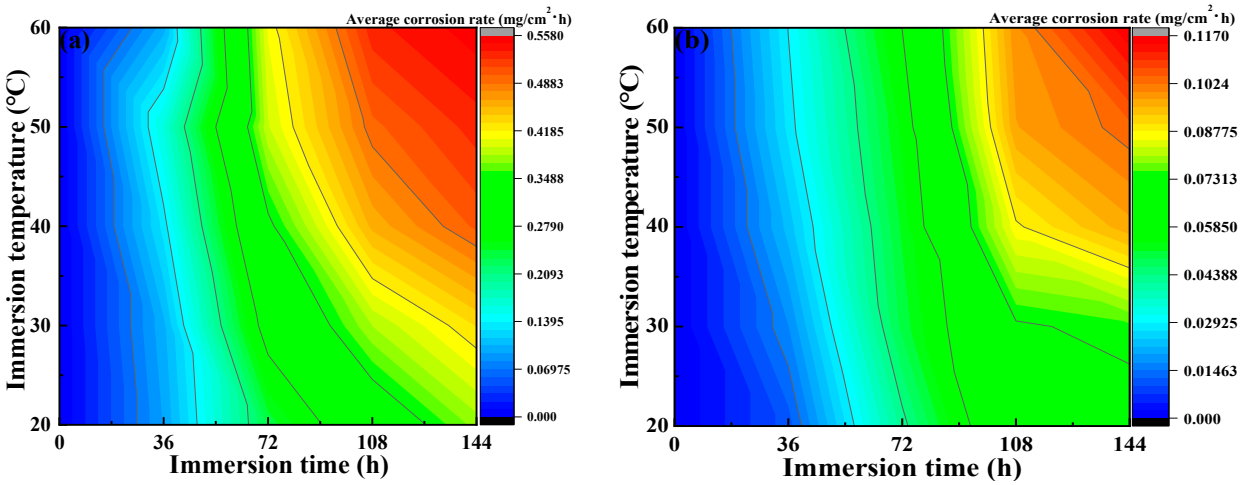


Figure 3. Polarization resistance of the Al alloy matrix, MoTiCC and MoTiZrCC.

3.4. Immersion Test

The immersion test, a typical accelerated test, has been extensively utilized to simulate the corrosion behavior of the aluminum alloy under severe working conditions. Figure 4 represents the average corrosion rate (ACR) of the Al alloy matrix and MoTiZrCC soaked in a neutral 3.5 wt.% NaCl solution under different immersion times and temperatures. It can be seen that the ACR increased with the increase in immersion temperature and immersion time. Normally, the increase in immersion temperature can improve the activity of corrosive Cl^{-1}, and then increase its probability of contact with the surface, thus increasing the ACR. As for the immersion time, it is closely related to the corrosion process. A sufficient immersion time also increases the contact time and probability of contact between corrosive Cl^{-1} and the surface of the Al alloy matrix, and thereby increases the ACR.



(a) Al alloy matrix (b) MoTiZrCC

Figure 4. Average corrosion rate of (**a**) the Al alloy matrix and (**b**) the MoTiZrCC versus the immersion time under different immersion temperatures.

Meanwhile, the ACR of the MoTiZrCC was obviously lower than that of the Al alloy matrix by comparison. To clearly distinguish the corrosion resistance between them, taking the immersion time of 144 h and the immersion temperature of 60 °C as an example, the ACRs of the Al alloy matrix and MoTiZrCC were 0.556 and 0.093 mg/cm^2·h, respectively. It was noticeable that the corrosion resistance of the MoTiZrCC was tremendously improved by nearly six times that of the Al alloy matrix. To sum up, immersion temperature and immersion time are two important factors that affect the corrosion process, and the MoTiZrCC can greatly improve the service life of the Al alloy matrix.

3.5. Morphology and Composition Analysis

3.5.1. SEM and EDS Analysis

The above results indicate that the MoTiZrCC has good corrosion resistance, and the micro-morphology and element content evolution of the MoTiZrCC are shown in Figures 5 and 6, respectively. As can be observed from Figure 5, some gaps appeared on the surface within the CTI of 8 min, and the introduction of the gaps was primarily due to the incomplete two-dimensional (2D) growth. Normally, such gaps often become channels for the corrosion medium to corrode the Al alloy matrix, leading to the decline in corrosion resistance. Owing to the growth of the CC, the width of the gaps gradually became smaller. As the CTI reached 12 min, the gaps basically disappeared and the surface was relatively flat. With the extension of CTI, some small gaps appeared on the surface due to local dissolution.

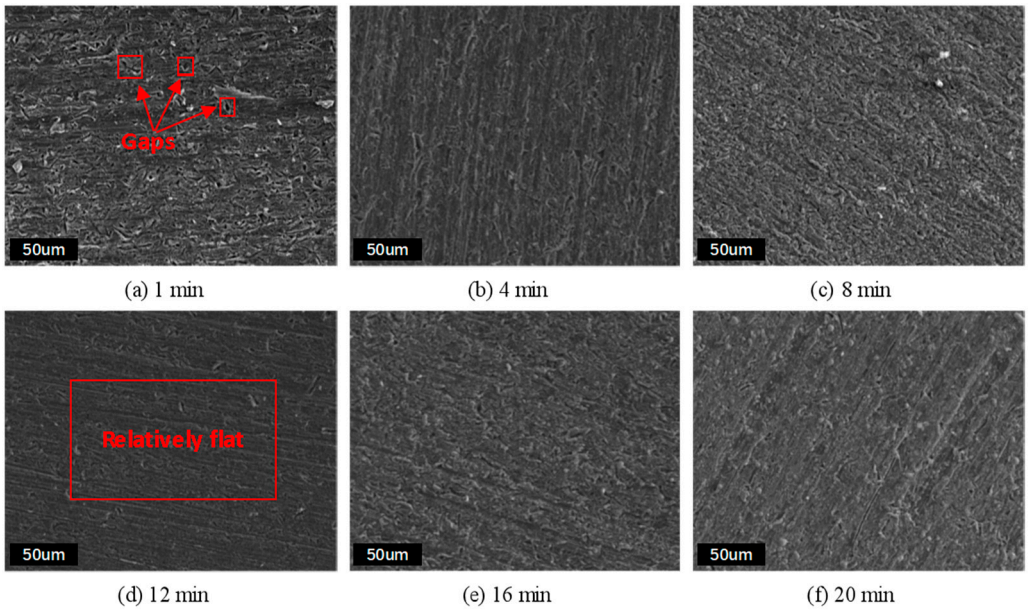


Figure 5. Scanning electron microscopy micrograph of the MoTiZrCC () with different CTIs, (**a**) 1 min, (**b**) 4 min, (**c**) 8 min, (**d**) 12 min, (**e**) 16 min and (**f**) 20 min. Note: the arrows point to the Gaps, and the box area represents that the area is relatively flat.

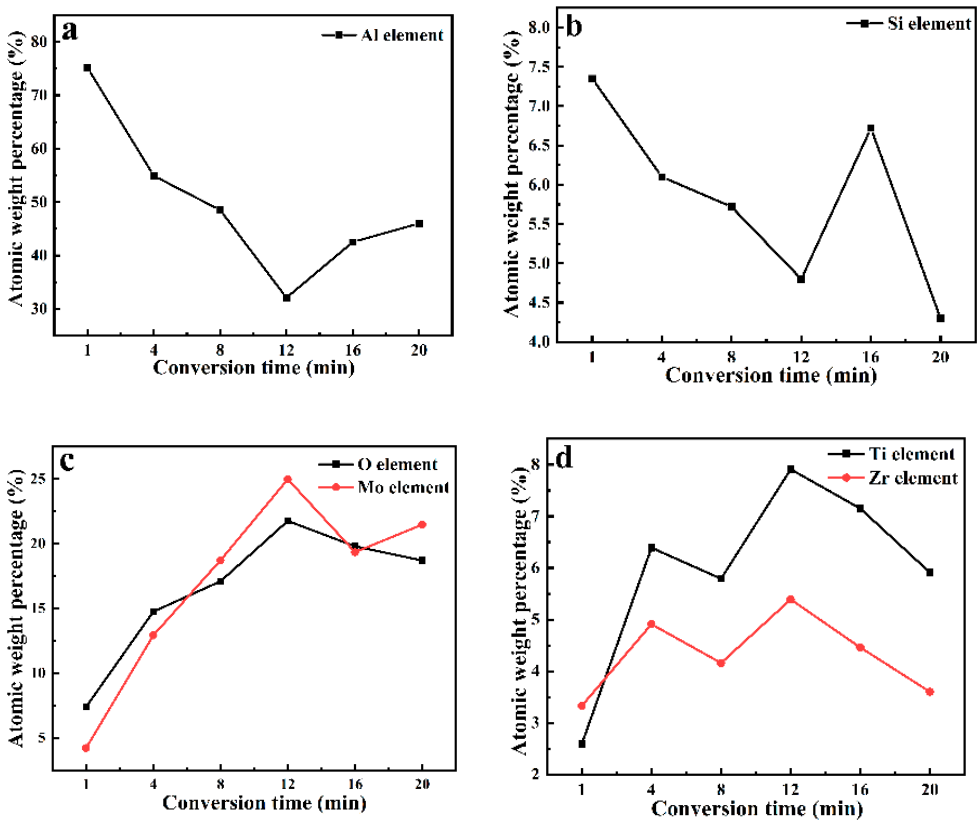


Figure 6. EDS analysis of the MoTiZrCC with different CTIs, (**a**) Al element, (**b**) Si element, (**c**) O and Mo elements and (**d**) Ti and Zr elements.

Figure 6 shows the atomic weight percentage of the main elements related to the MoTiZrCC with different CTIs, and there were mainly seven elements including Al, Si, O, Mo, Ti, and Zr on the surface. The Al and Si elements (Figure 6a,b) were the constituent elements of the Al alloy matrix, and the overall trend of their content declined with the

extension of CTI due to the growth of the MoTiZrCC and the local dissolution of the Al alloy matrix on the surface. Correspondingly, Mo, Ti, Zr and O (Figure 6c,d), the four elements forming the MoTiZrCC, had the opposite trend of the Al and Si elements.

It is noteworthy that the maximum content of the MoTiZrCC constituent elements and the minimum content of the Al alloy matrix constituent elements both appeared in the CTI of 12 min, showing that the MoTiZrCC constituent elements had deposited well onto the surface under that CTI. Interestingly, the micro-morphology with a relatively flat and dense surface also appeared in the CTI of 12 min from the SEM analysis. Therefore, it can be exactly verified that the MoTiZrCC with the CTI of 12 min grows fully, and thus has good corrosion resistance.

3.5.2. XPS Analysis

XPS was utilized to characterize the detailed information relevant to the elemental valence states and types of compounds, and the total spectrum of the MoTiZrCC with the CTI of 12 min is shown in Figure 7. The results confirmed the presence of Mo, Ti, Zr, Al, O, F and C on the surface, and they were basically consistent with the EDS results. Additionally, the tiny C1s peak of 284.8 eV used to correct the total XPS spectrum may originate from the impurities and surfactant, and we omitted to perform a detailed analysis.

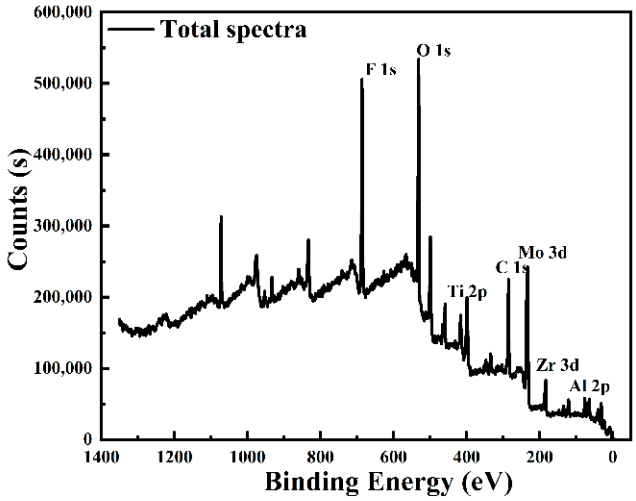


Figure 7. XPS total spectrum of MoTiZrCC with the CTI of 12 min.

To accurately identify the different types of compounds on the surface, the high-resolution XPS spectra of Al 2p, O 1s, Mo 3d, Ti 2p, Zr 3d and F 1s and their fitting peaks were carried out, as shown in Figure 8a–f, respectively. The Al 2p spectrum (Figure 8a) can be deconvoluted into two peaks: the peak located at 75.87 eV is related to Al_2O_3; the peak located at 76.19 eV is related to $AlF_3{\cdot}3H_2O$. The fitting results of the O 1s spectrum (Figure 8b) exhibit two peaks at about 530.53 and 531.66 eV. The binding energy of 530.53 eV is assigned to MoO_3, TiO_2 and ZrO_2, and the other peak corresponds to Al_2O_3.

The peaks of the Mo 3d spectrum (Figure 8c) can be fitted into four peaks: the peaks located at 232.84 and 236.09 eV are attributed to MoO_3, and the peaks located at 231.74 and 235.41 eV are attributed to Mo_2O_5. The split peaks of Ti 2p (Figure 8d) can be fitted into two peaks located at 464.77 and 458.91 eV, which are both associated with TiO_2. The two peaks (Figure 8e) of Zr 3d at 182.89 and 185.21 eV are ascribed to ZrO_2 and ZrF_4.

Additionally, the fitting results of the F 1s spectrum (Figure 8f) exhibit two peaks: the peak located at 685.43 is assigned to Na_3AlF_6; the other peak located at 686.12 is assigned to ZrF_4. In summary, the MoTiZrCC mainly consists of a series of metallic oxides, such as MoO_3, Mo_2O_5, TiO_2, ZrO_2, Al_2O_3, and small amounts of metallic fluorides such as Na_3AlF_6, ZrF_4 and $AlF_3{\cdot}3H_2O$.

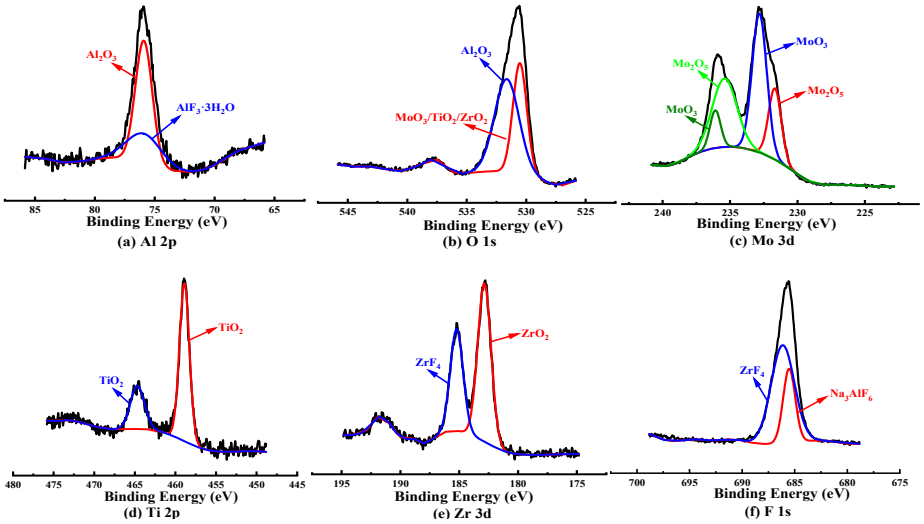


Figure 8. The high-resolution XPS spectra of MoTiZrCC with the CTI of 12 min, (**a**) Al 2p, (**b**) O 1s, (**c**) Mo 3d, (**d**) Ti 2p, (**e**) Zr 3d and (**f**) F 1s.

3.6. Formation Mechanism of MoTiZrCC

Generally, the MoTiZrCC constituent elements were preferentially adsorbed in certain regions to form nucleation centers at the initial stage due to the uneven distribution of various phases in the Al alloy matrix. In order to determine the preferential deposition region, the elemental distribution of MoTiZrCC with the short CTI of 0.5 min was achieved using the area scan by EDS, as shown in Figure 9. Among them, the distribution of the Mg element was relatively uniform. However, some micro-regions (preferential deposition region) were rich in Mo, Ti and Zr elements, and the content of Al, Cu and Si elements in this region was relatively low, which verifies that the MoTiZrCC was preferentially deposited on the Al-Si-Cu intermetallic compound [29]. Therefore, nucleation usually occurred near the intermetallic compounds used as the micro-cathode, while the Al-rich matrix was used as the micro-anode.

Based on the SEM, EDS and XPS characterizations, the formation mechanism of the MoTiZrCC on the Al alloy matrix is discussed as follows:

In the natural environment, the Al alloy matrix is spontaneously covered with a thin and discontinuous layer of Al_2O_3 in the atmosphere [30,31], which has poor stability, as shown in Figure 10a. So as to improve the surface activity, the Al alloy matrix was abraded with emery paper and then washed with 5% ZHM-1026 to remove the naturally formed oxide film and grease.

Immediately, the fresh bare surface was immersed in the conversion solution and underwent a complex film-forming process. Once the Al alloy contacts the conversion solution, the Al-rich matrix (micro-anode) is dissolved to produce Al^{3+} ions, accompanied by the liberation of electrons [32], as shown in Equation (3). Meanwhile, because of abundant hydrogen ions and H_2O molecules near the intermetallic compound region (micro-cathode), these electrons are accepted by two paths: (1) the H^+ ion receives electrons to form H_2 (g) as shown in Equation (4); (2) the H_2O and dissolved oxygen in the electrolyte receive electrons to generate OH^- ions, as shown in Equation (5).

Micro-anode

$$Al - 3e^- \rightarrow Al^{3+} \quad (3)$$

Micro-anode

$$2H^+ + 2e^- \rightarrow H_2 \uparrow \quad (4)$$

$$O_2 + 2H_2O + 4e^- \rightarrow 4OH^- \quad (5)$$

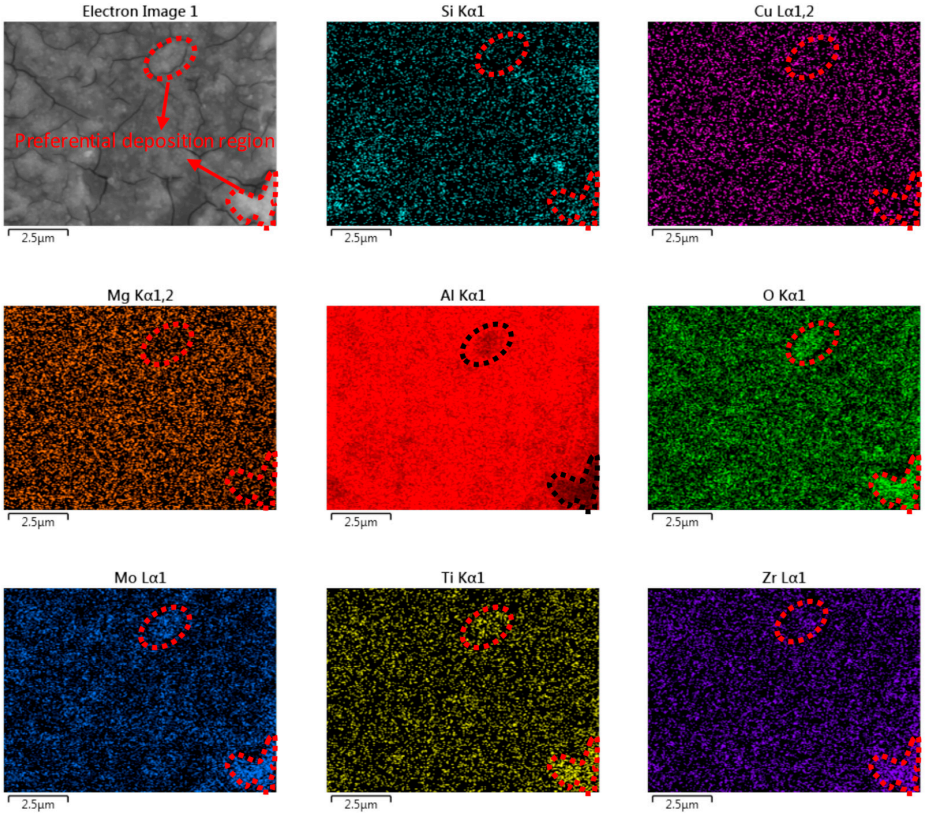


Figure 9. Elemental distribution of the MoTiZrCC with the CTI of 0.5 min.

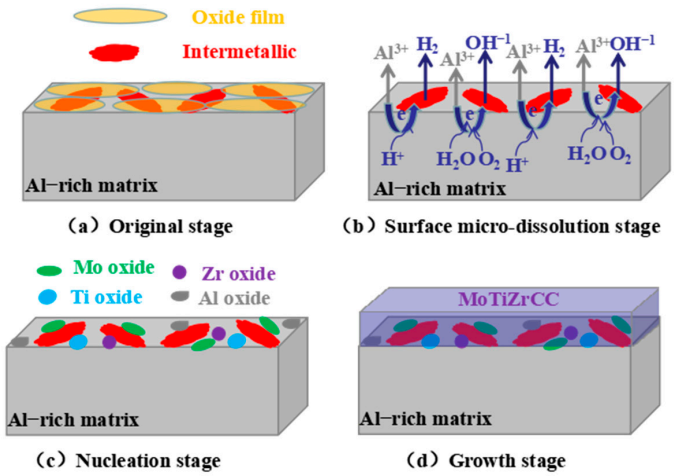


Figure 10. The schematic diagrams of the growth process, (**a**) Original stage, (**b**) Surface micro-dissolution stage, (**c**) Nucleation stage and (**d**) Growth stage.

Hydrogen evolution and oxygen absorption reactions can cause a pH rise at the solution/Al alloy matrix interface. This causes the released free Al^{3+} to positively combine with the OH^- to form poorly soluble $Al(OH)_3$ on the surface, and further transform to Al_2O_3 after dehydration, as shown in Equation (6). Simultaneously, MoO_4^{2-}, TiF_6^{2-} and $TiZr_6^{2-}$ in the conversion solution are adsorbed on the surface and react to produce the nucleation centers of the corresponding metal oxides near the intermetallic compound region, as shown in Equations (7)–(10). The schematic diagram of the nucleation process relevant to the various metal oxides is shown in Figure 10c.

$$Al^{3+} + 3OH^- \rightarrow Al(OH)_3 \rightarrow Al_2O_3 \quad (6)$$

$$2MoO_4^{2-} + 2e^- + 6H^+ \rightarrow Mo_2O_5 + 3H_2O \quad (7)$$

$$MoO_4^{2-} + 2H^+ \rightarrow MoO_3 + H_2O \quad (8)$$

$$TiF_6^{2-} + 4OH^- \rightarrow TiO_2 \cdot 2H_2O + 6F^- \quad (9)$$

$$ZrF_6^{2-} + 4OH^- \rightarrow ZrO_2 \cdot 2H_2O + 6F^- \quad (10)$$

After the nucleation center was formed, its epitaxy constantly adsorbed new metal oxides generated by the conversion reaction to reduce the surface energy, thus leading to its rapid growth. The growth pattern was mainly two-dimensional plane growth, and the thickness direction growth rate was slow due to high internal growth stress. After a period of growth, a complete MoTiZrCC was finally formed on the surface, as shown in Figure 10d. To sum up, the growth process of the MoTiZrCC mainly goes through four stages: pretreatment stage, surface micro-dissolution stage, nucleation stage and growth stage.

4. Conclusions

The optimal conversion parameters of pH and CTI were 4.5 and 12 min respectively, and the addition of Na_3VO_4 had little effect on the improvement of corrosion resistance. The addition of H_2ZrF_6 could significantly improve the corrosion resistance, and the most appropriate addition amount was 1.2 mL/L.

The surface of the MoTiZrCC under the optimal conversion parameters was relatively uniform and dense, and the gaps associated with the corrosion resistance also basically disappeared. The MoTiZrCC mainly consists of Mo, Ti, Zr, Al, F and O elements, and its main phases are MoO_3, Mo_2O_5, TiO_2, ZrO_2 and Al_2O_3, as well as a small quantity of Na_3AlF_6 and $AlF_3 \cdot 3H_2O$.

The MoTiZrCC achieved a lower I_{corr} and a more positive E_{corr} and R_p, and the corrosion resistance was improved by nearly six times in contrast to the Al alloy matrix. The region near the intermetallic compound was the preferential deposition region, and the four stages of the formation mechanism relevant to MoTiZrCC were proposed.

Author Contributions: Conceptualization, W.Z.; methodology, X.Q. and W.Z.; writing—original draft preparation software, X.Q., F.H., X.T. and W.Z.; investigation and data curation, X.Q., F.H. and W.Z.; software, X.Q., F.H., X.T., Y.W. and W.Z.; writing—reviewing and editing, Y.F., J.P., W.W. and Y.L. All authors have read and agreed to the published version of the manuscript.

Funding: This work was supported by National Natural Science Foundation of China (52075391); Natural Science Foundation of Anhui Higher Education Institutions (KJHS2020B09); Open fund of State Key Laboratory of tribology, Tsinghua University (SKLTKF20B07); Talent research start-up fund of Huangshan University (2018xkjq003); Open project of Anhui Simulation Design and Modern Manufacturing Engineering Technology Research Center (SGCZXYB2001).

Data Availability Statement: Not applicable.

Conflicts of Interest: The authors declare no conflict of interest.

References

1. Wang, H.; Ou, X.; Zhang, X. Mode, technology, energy consumption, and resulting CO2 emissions in China's transport sector up to 2050. *Energ. Policy* **2017**, *109*, 719–733. [CrossRef]
2. Hosseinzadeh, F.; Rastegar, S.; Ashengroph, M. Bioleaching of rare earth elements from spent automobile catalyst as pretreatment method to improve Pt and Pd recovery: Process optimization and kinetic study. *Proc. Biochem.* **2021**, *105*, 1–7. [CrossRef]
3. Wu, Y.; Zhang, S.; Hao, J.; Liu, H.; Wu, X.; Hu, J.; Walsh, M.; Wallington, T.; Zhang, K.; Stevanovic, S. On-road vehicle emissions and their control in China: A review and outlook. *Sci. Total. Environ.* **2017**, *574*, 332–349. [CrossRef]
4. Zhou, J.; Wang, F.; Wan, X. Optimal Design and Experimental Investigations of Aluminium Sheet for Lightweight of Car Hood. *Mater. Today Proc.* **2015**, *2*, 5029–5036. [CrossRef]
5. Iqbal, M.; Sun, L.; Lachance, A.; Ding, H.; Fedel, M. In situ growth of a CaAl-NO_3-layered double hydroxide film directly on an aluminum alloy for corrosion resistance. *Dalton. Trans.* **2020**, *49*, 3956–3964. [CrossRef]
6. Liu, Y.; Zhu, B.; Wang, K.; Li, S.; Zhang, Y. Friction behaviors of 6061 aluminum alloy sheets in hot stamping under dry and lubricated conditions based on hot strip drawing test. *Tribol. Int.* **2020**, *151*, 106504. [CrossRef]

7. Xiao, W.; Wang, Y. Corrosion Resistance of Aluminum Fluoride Modified 6061 Aluminum Alloy. *Mater. Lett.* **2021**, *298*, 129932. [CrossRef]
8. El-Meligi, A.; Sanad, S.; Ismail, A.; Barakat, A. Corrosion penetration and crystal structure of AA5022 in HCl solution and rare earth elements. *J. Mater. Sci. Technol.* **2005**, *21*, 324–330. [CrossRef]
9. Nicolo, A.; Paussa, L.; Gobessi, A.; Lanzutti, A.; Cepek, C.; Andreatta, F.; Fedrizzi, L. Cerium conversion coating and sol–gel multilayer system for corrosion protection of AA6060. *Surf. Coat. Tech.* **2016**, *287*, 33–43. [CrossRef]
10. Zhan, W.; Li, X.; Qian, X.; Li, Y.; Ding, Y.; Zu, Y.; Xie, F.; Tian, F. Preparation and Characterization of Synchronous Chemical Conversion Coating on 6061 Aluminum Alloy/7075 Aluminum Alloy/Galvanized Steel Substrates. *Metals* **2022**, *12*, 2011. [CrossRef]
11. Díaz, B.; Freire, L.; Mojío, M.; Novoa, X. Optimization of conversion coatings based on zinc phosphate on high strength steels, with enhanced barrier properties. *J. Electroanal. Chem.* **2015**, *737*, 174–183. [CrossRef]
12. Mahidashti, Z.; Shahrabi, T.; Ramezanzadeh, B. A new strategy for improvement of the corrosion resistance of a green cerium conversion coating through thermal treatment procedure before and after application of epoxy coating. *Appl. Surf. Sci.* **2016**, *390*, 623–632. [CrossRef]
13. Roshan, S.; Sarabi, A. Improved performance of Ti-based conversion coating in the presence of Ce/Co ions: Surface characterization, electrochemical and adhesion study. *Surf. Coat. Tech.* **2021**, *410*, 126931. [CrossRef]
14. Zhang, X.; Yin, Z.; Buhe, B.; Wang, J.; Mao, L.; Liu, B.; Zhou, P.; Zhao, Y.; Zhang, T.; Wang, F. Effect of Temperature on Corrosion Resistance of Layered Double Hydroxides Conversion Coatings on Magnesium Alloys Based on a Closed-Cycle System. *Metals* **2021**, *11*, 1658. [CrossRef]
15. Munson, C.; McFall-Boegeman, S.; Swain, G. Cross comparison of TCP conversion coating performance on aluminum alloys during neutral salt-spray and thin-layer mist accelerated degradation testing. *Electrochim. Acta* **2018**, *282*, 171–184. [CrossRef]
16. Qian, X.; Zhao, W.; Zhan, W.; Zhang, T.; Pan, J.; Liu, Y. Formation and corrosion resistance of a novel Co-Ti-Mo composite chromium-free chemical conversion coating on LY12 aluminum alloy. *Mater. Corros.* **2022**, *73*, 710–719. [CrossRef]
17. Bouali, A.; Serdechnova, M.; Blawert, C.; Tedim, J.; Ferreira, M.; Zheludkevich, M. Layered double hydroxides (LDHs) as functional materials for the corrosion protection of aluminum alloys: A review. *Appl. Mater. Today* **2020**, *21*, 100857. [CrossRef]
18. Gu, Y.; Wang, S.; Xu, S. Preparation and adhesive properties of colored Ti/Zr-based conversion coating on aluminum foil for lithium battery packaging. *Surf. Interface. Anal.* **2019**, *51*, 190–198. [CrossRef]
19. Coloma, P.; Izagirre, U.; Belaustegi, Y.; Jorcin, J.; Canoa, F.; Lapeña, N. Chromium-free conversion coatings based on inorganic salts (Zr/Ti/Mn/Mo) for aluminum alloys used in aircraft applications. *Appl. Surf. Sci.* **2015**, *345*, 24–35. [CrossRef]
20. Alba-Galvín, J.J.; González-Rovira, L.; Botana, F.J.; Lekka, M.; Andreatta, F.; Fedrizzi, L.; Bethencourt, M. Application of Commercial Surface Pretreatments on the Formation of Cerium Conversion Coating (CeCC) over High-Strength Aluminum Alloys 2024-T3 and 7075-T6. *Metals* **2021**, *11*, 930. [CrossRef]
21. Balaraju, J.; Srinivasan, A.; Yoganandan, G.; Grips, V.; Rajam, K. Effect of Mn/Mo incorporated oxide layer on the corrosion behavior of AA 2024 alloy. *Corros. Sci.* **2011**, *53*, 4084–4092. [CrossRef]
22. Becker, M. Chromate-free chemical conversion coatings for aluminum alloys. *Corros. Rev.* **2019**, *37*, 321–342. [CrossRef]
23. Qian, X.; Zhan, W.; Pan, J.; Liu, Y.; Huang, F.; Wang, B. Improving the corrosion resistance of LY12 aluminum alloy via a novel Mo-Zr-Ti composite conversion coating. *Mater. Res. Express.* **2021**, *8*, 036403. [CrossRef]
24. Cerezo, J.; Taheri, P.; Vandendael, I.; Posner, R.; Lill, K.; Wit, J.; Mol, J.; Terryn, H. Influence of surface hydroxyls on the formation of Zr-based conversion coatings on AA6014 aluminum alloy. *Surf. Coat. Tech.* **2014**, *254*, 277–283. [CrossRef]
25. Guo, G.; Song, D.; Jiang, J.; Ma, A.; Zhang, L.; Li, C. Effect of Synthesizing Temperature on Microstructure and Electrochemical Property of the Hydrothermal Conversion Coating on Mg-2Zn-0.5Mn-Ca-Ce Alloy. *Metals* **2016**, *6*, 44. [CrossRef]
26. Song, D.; Lian, B.; Fu, Y.; Wang, G.; Qiao, Y.; Klu, E.E.; Gong, X.; Jiang, J. Dual-Layer Corrosion-Resistant Conversion Coatings on Mg-9Li Alloy via Hydrothermal Synthesis in Deionized Water. *Metals* **2021**, *11*, 1396. [CrossRef]
27. Duan, H.; Yan, C.; Wang, F. Effect of electrolyte additives on performance of plasma electrolytic oxidation films formed on magnesium alloy AZ91D. *Electrochim. Acta* **2007**, *52*, 3785–3793. [CrossRef]
28. Yin, Z.; Huang, W.; Song, X.; Zhang, Q.; Zeng, R. Self-catalytic degradation of iron-bearing chemical conversion coating on magnesium alloys-Influence of Fe content. *Front. Mater. Sci.* **2020**, *3*, 296–313. [CrossRef]
29. Cerezo, J.; Vandendael, I.; Posner, R.; Wit, J.; Mol, J.; Terryn, H. The effect of surface pre-conditioning treatments on the local composition of Zr-based conversion coatings formed on aluminium alloys. *Appl. Surf. Sci.* **2016**, *366*, 339–347. [CrossRef]
30. Zhang, P.; Wang, Y.; Li, W.; Wang, Q.; Li, Y. A study on microstructure evolution and corrosion resistance of cutting layer metal of 7055 aluminum alloy based on extreme environment. *Mater. Corros.* **2017**, *69*, 1389–1397. [CrossRef]
31. Oger, L.; Lafouresse, M.; Odemer, G.; Peguet, L.; Blanc, C. Hydrogen diffusion and trapping in a low copper 7xxx aluminium alloy investigated by Scanning Kelvin Probe Force Microscopy. *Mat. Sci. Eng. A* **2017**, *706*, 126–135. [CrossRef]
32. Ahmadi, P.; Sarabi, A.; Mohammadloo, H.; Behgam, R. Effect of practical parameters on the structure and corrosion behavior of vanadium/zirconium conversion coating on AA 2024 aluminum alloy. *J. Coat. Technol. Res.* **2019**, *6*, 1503–1513. [CrossRef]

Disclaimer/Publisher's Note: The statements, opinions and data contained in all publications are solely those of the individual author(s) and contributor(s) and not of MDPI and/or the editor(s). MDPI and/or the editor(s) disclaim responsibility for any injury to people or property resulting from any ideas, methods, instructions or products referred to in the content.